Adaptive Parameter Tuning and Virtual Impedance Injection Control for Coupled Harmonic Mitigation of Photovoltaic Converter

Pengbo Shan, *Student Member, IEEE*, Yuanyuan Sun, *Senior Member, IEEE*, Yuanzong Song, Fan Zhang, Yahui Li, *Member, IEEE*, and Kaiqi Sun, *Member, IEEE*

***Abstract*—Suppressing current harmonics is an essential issue for photovoltaics (PVs). The equivalent impedance or admittance expresses the interaction between the PV converter (PVC) and the background harmonics from the grid, where the control strategies and parameters play a crucial role in the process. Currently, multifrequency coupling characteristics have become more vital in harmonic analysis, and traditional selective harmonic suppression methods show imperfect performance. The key to solving this issue is constructing an adaptive controller for coupled harmonic mitigation according to grid conditions. Therefore, this article first constructs a harmonic coupling matrix model (HCMM) of the PVC to describe the harmonic coupling characteristics, which can represent the influence of topology and control parameters simultaneously. Second, the effect of the critical controller parameters and virtual impedance method on the coupled harmonic admittance of the HCMM is analyzed. Finally, coordinated control of adaptive parameter tuning and virtual impedance injection method is proposed to reduce coupled harmonics efficiently and to avoid the instability caused by the modulation voltage saturation. Comparative experiments are provided by a three-phase PVC with a digital signal processing (DSP) controller, and the results verify the validity of the coupled harmonic analysis and the effectiveness of the proposed method.**

***Index Terms*—Coupled harmonic mitigation, harmonic coupling, photovoltaic converter (PVC), stability of the control system, virtual impedance.**

I. Introduction

HARMONICS in the distribution network are significantly increasing due to the massive amount of distributed photovoltaic (PV) [1]. Compared with traditional power, PV completes ac and dc power transmission through a PV converter (PVC), which is designed to operate in ideal scenarios. However, complex harmonics are generated by PVCs under nonideal supply conditions [2]. These harmonics beyond expectations cause numerous accidents, such as power outages, medical and household electrical appliance burns, etc., which limits the ability of the distribution system to accept a more significant scale of renewable energy. Therefore, harmonic mitigation of the PVC is an urgent issue for the quality supply of the current distribution system [3], [4], [5].

Harmonic sources in traditional distribution systems are relatively centralized, and passive or active power filters (APFs) are installed to avoid harmonic exceeding limits [6], [7]. This approach is limited by the significant financial investment. Furthermore, with PVCs scattered access to new distribution systems, harmonic sources are located in separate areas. It is hard to configure enough filters due to the economic operation principle. Currently, although PVC is not an ideal power, the harmonic injected into the system can be suppressed through control optimization without installing additional filters [8]. Furthermore, it has become a hot research topic to make PVCs produce ideal waveforms in various nonideal conditions.

The nonideal switching characteristic of the converter is an essential reason for the low-order harmonics [9]. Therefore, multiple methods have been proposed to make converters exhibit nearly idealized switching characteristics, such as the lookup table method [10], online compensation [11], and optimized time sequence control [12], etc. These studies have shown that harmonic reduction can be achieved by changing the modulation signal [13]. However, the same performance of these methods is hard to guarantee with background harmonics increasing. Therefore, to mitigate harmonics in such nonideal scenarios sufficiently, many scholars have developed the PVC to perform as an APF [14], [15]. These strategies may provide fluctuating suppression results under different weather due to the deficient capacity of the PVC and harmonic phase mismatch [16]. In summary, the above methods achieve different levels of harmonic mitigation performance but have restricted application scenarios.

In contrast, virtual impedance control is a more effective harmonic mitigation method for nonideal supply scenarios. In many models, harmonic impedance or admittance are used to describe the characteristic that PVC generates harmonic current due to background harmonics [17]. If the harmonic coupling is not considered, constructing virtual impedance between PVC and grid can effectively suppress the selective harmonics [18]. In addition, virtual impedance is more beneficial to keep the control system stabilized compared with virtual resistance and

Received 6 March 2024; revised 3 July 2024; accepted 18 August 2024. Date of publication 23 August 2024; date of current version 12 December 2024. This work was supported by the National Natural Science Foundation of China under Grant U23B20116 and Grant 523B2075. Recommended for publication by Associate Editor D. Dong. *(Corresponding author: Yuanyuan Sun.)*

The authors are with the School of Electrical Engineering, Shandong University, Jinan, Shandong 250100, China (e-mail: 202220672@mail.sdu.edu.cn; sunyy@sdu.edu.cn; songyuanzong@mail.sdu.edu.cn; 202234721@mail.sdu.edu.cn; liyahui@sdu.edu.cn; skq@sdu.edu.cn).

Color versions of one or more figures in this article are available at https://doi.org/10.1109/TPEL.2024.3449080.

Digital Object Identifier 10.1109/TPEL.2024.3449080

capacitance due to its phase lead characteristic [19]. To reduce the complexity of the design due to the harmonic transformation relationship between the ac and the dc side, a current suppression method based on impedance editing for the dc side of the voltage source converter is proposed [20]. Unfortunately, the previous research almost ignores the harmonic coupling characteristic, few research has been found on virtual impedance control strategy for coupled harmonic mitigation. However, the coupled harmonic percentage of PVC can reach 15% to 30% [21], and the coupled components may be amplified due to the virtual impedance injection at the chosen frequency. Therefore, the complex challenges caused by the harmonic coupling characteristic cannot be ignored.

In summary, harmonic suppression of PVC at distorted supply voltages is still challenging. The crucial suppression performance is determined by the influence of the control method and operating parameters on the harmonic coupling characteristics. The existing techniques are adapted to specific scenarios and can't adaptively accomplish coupled harmonics mitigation, remaining a considerable improvement space in distribution systems with variable background harmonics.

To overcome the above research gaps, this article focuses on the coupled harmonic mitigation of PVC. It is found that not only the topology and control but also the harmonic mitigation strategy contributes to the harmonic coupling characteristic. The contributions of this article are summarized as follows.

1) To analyze the coupling characteristics of PVC, the harmonic coupling matrix model (HCMM) is established based on control and topology parameters. The matrix dimension is simplified by numerous frequency scanning experiments.
2) The corresponding regularity of control parameters on harmonic characteristics of PVC are analyzed. To minimize harmonics before virtual impedance injection, the most influential parameter K_{pi} is selected to guide the controller parameter optimal tunning.
3) Performances of different virtual impedances on coupled harmonics are analyzed to propose the adaptive virtual impedance injection method. Under random conditions, the proposed method minimizes the coupled harmonics without damaging control stability compared with the traditional methods.

The rest of the article is organized as follows. Section II describes the HCMM of the PVC. Section III shows the analysis of the controller parameters on harmonic coupling. The change of HCMM due to the virtual impedance control is discussed in Section IV. A coordinated control of adaptive parameter tuning and virtual impedance injection method is proposed in Section V, and comparative experiments are shown in Section VI. Finally, Section VII concludes this article.

II. HCMM Modeling of PVC

The harmonic coupling matrix is defined by the harmonic state-space (HSS) model in this article, and the model is separated into two parts.

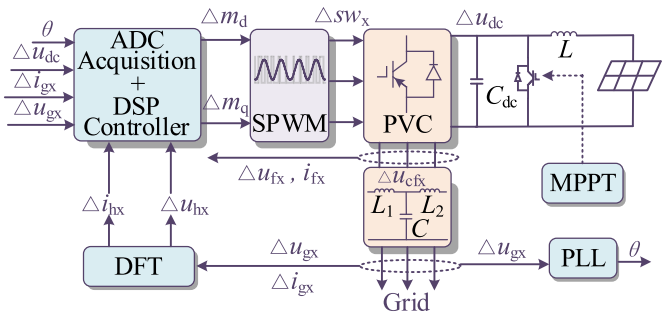

Fig. 1. Typical topology of the PVC.

1) The topology model expresses the ac and dc energy transmission.
2) The controller model expresses the pulsewidth modulation (PWM) switching functions.

Section II-A and II-B describes the modeling process above separately, and Section II-C introduces the coupling characteristics described by the HCMM.

A. Topology Modeling

Fig. 1 shows the typical topology of a PVC with an *LCL* filter, and the whole system is nonlinear time-varying. It is linearized at a steady state in a minimum linearization period $[t_0,\ t_0+T_s]$ to describe its linear periodic time-varying (LPT) harmonic characteristics, where T_s is the control and sampling period. Therefore, the small-signal representation (Δ) is used in the linearized model to establish the time-domain differential equations. The physical connection between the ac side of PVC and the grid voltage is derived into differential equations of the *LCL* filter in

$$\begin{cases} L_1 \frac{d\Delta i_{fx}}{dt} = \Delta u_{fx} - \Delta u_{cfx} \\ L_2 \frac{d\Delta i_{gx}}{dt} = \Delta u_{cfx} - \Delta u_{gx} \\ C \frac{d\Delta u_{cfx}}{dt} = \Delta i_{fx} - \Delta i_{gx} \end{cases}, x = (a,b,c) \tag{1}$$

where Δi_{gx} and Δu_{gx} are grid-connected current and voltage, Δi_{fx} and Δu_{fx} are output current and voltage, L_1, L_2, and C are parameters of the *LCL* filter, and Δu_{cfx} is the voltage of the filter capacitor.

The energy transfer relationship of the ac and dc sides of the PVC is connected by the switching function ($\Delta \mathrm{sw}_x$). The linear time-varying characteristics of the ac–dc transformation process are presented as

$$\Delta i_{\mathrm{dc}} = C_{\mathrm{dc}} \frac{d}{dt} \Delta u_{\mathrm{dc}} = \sum_{x=a,b,c} \Delta i_{fx} \tilde{s} w_x + \sum_{x=a,b,c} \tilde{i}_{fx} \Delta \mathrm{sw}_x$$

$$\Delta u_{fx} = \Delta u_{\mathrm{dc}} \tilde{s} w_x + \tilde{u}_{\mathrm{dc}} \Delta \mathrm{sw}_x \tag{2}$$

where $\Delta \mathrm{sw}_x$ is the switching function, C_{dc} is the capacitor of the dc side, Δu_{dc} and Δi_{dc} are the voltage and current of this capacitor. The superscript "$\sim$" in (2) means a previous state value before the current control cycle.

Another assumption is that the harmonic characteristics of PVC is linear time-varying periodically at an equilibrium state.

According to this assumption, the PVC can be modeled by a state space matrix in (3). The LPT varying theory transfers time-domain variables in (3) to the frequency domain in (4) by bilateral Fourier decomposition [22].

$$\dot{x}(t) = A(t)x(t) + B(t)u(t) \tag{3}$$

$$\begin{cases} x(t) = e^{st}\sum_{h=-\infty}^{\infty} x_h e^{jh\omega_0 t}, \dot{x}(t) = (jh\omega_0 + s)x(t) \\ u(t) = e^{st}\sum_{h=-\infty}^{\infty} u_h e^{jh\omega_0 t} \\ A(t) = e^{st}\sum_{h=-\infty}^{\infty} A_h e^{jh\omega_0 t}, B(t) = e^{st}\sum_{h=-\infty}^{\infty} B_h e^{jh\omega_0 t} \end{cases} \tag{4}$$

where h is the harmonic order, and ω_0 is the grid frequency angular velocity.

To avoid confusion between multiple variables (h) in the multiplication operation, two independent variables (m and n) are used to separate the frequency of interaction in the process of obtaining (5). According to the harmonic balance principle, the coefficients of the same frequency components on both sides are equal, and they should satisfy $\delta = m + n$, the state space model of each frequency can be shown in (6)

$$\begin{aligned} &(j\delta\omega_0 + s)\sum_{\delta=-\infty}^{\infty} x_\delta e^{(j\delta\omega_0+s)t} \\ &= \sum_{m,n=-\infty}^{\infty} (A_m x_n + B_m u_n) e^{[j(m+n)\omega_0+s]t} \end{aligned} \tag{5}$$

$$(s + j\delta\omega_0)x_\delta = \sum_{m\in Z} A_{\delta-m}x_m + \sum_{m\in Z} B_{\delta-m}u_m \tag{6}$$

where δ is the analyzed harmonic order.

The state space model can be shown in (7) by associating the harmonic state equations at all frequencies to be considered

$$\begin{cases} sX_T = (A_\mathrm{T} - Q)X_T + B_T U_T \\ X_T = [\Delta i_{ga}, \Delta i_{gb}, \Delta i_{gc}, \Delta u_{ga}, \Delta u_{gb}, \Delta u_{gc}, \Delta u_\mathrm{dc}]^T \\ U_T = [\Delta u_{ga}, \Delta u_{gb}, \Delta u_{gc}, \Delta \mathrm{sw}_a, \Delta \mathrm{sw}_b, \Delta \mathrm{sw}_c]^T \end{cases} \tag{7}$$

where A_T and B_T are the state and input matrix of the topology state space model, $Q = \mathrm{diag}(-jH\omega_0 I \ldots -j\omega_0 I, Z_\mathrm{M}, j\omega_0 I \ldots jH\omega_0 I)$, Z_M and I are H-order zero matrix and unit matrix, and H is the maximum harmonic order to be considered.

Obviously, each small signal state variable in (7) contains H-order harmonic information. For example, any variable Δf ($f = i_{gx}$, u_{gx}, u_dc, $x =$ a, b, c) can be shown as

$$\Delta f = (f_{-H}, \ldots, f_0, \ldots, f_H). \tag{8}$$

When the PVC is operating at a steady state, the signals in two continuous periods are approximately equal. Therefore, assuming that $sX_T = 0$ in the linearization period and the harmonic transfer matrix (HTM) can be shown in (9). Every element of HTM represents the harmonic interaction between two frequencies in X_T and U_T. The HSS topology model of PVC can be expressed as

$$H_T = -(A_T - N)^{-1}B_T = H_{Ta} + H_{Tb} \tag{9}$$

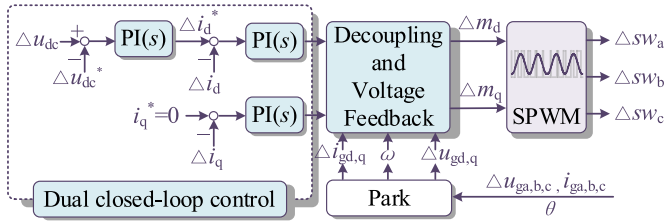

Fig. 2. Typical control of the PVC.

where H_{Ta} and H_{Tb} are transfer matrices of voltage and switching function separately

$$\begin{pmatrix} \Delta i_{ga} \\ \Delta i_{gb} \\ \Delta i_{gc} \\ \Delta u_{dc} \end{pmatrix} = H_{Ta}\begin{pmatrix} \Delta u_{ga} \\ \Delta u_{gb} \\ \Delta u_{gc} \end{pmatrix} + H_\mathrm{Tb}\begin{pmatrix} \Delta \mathrm{sw}_a \\ \Delta \mathrm{sw}_b \\ Dsw_c \end{pmatrix}. \tag{10}$$

B. Controller Modeling

In Section II-, Fig. 2 shows typical control of the PVC. The outer loop maintains the dc voltage stability, and the inner loop realizes fast current tracking. The PWM signals determine the switching state of the insulated gate bipolar transistor.

The controller of the PVC contains three proportional-integral (PI) controllers whose functions are PI(s) = $K_p + K_i/s$. State variables are set in (8) to quantify the effect of the integration module on each frequency

$$\dot{X}_v = \Delta u_\mathrm{dc} - \Delta u_\mathrm{dc}^*, \dot{X}_{id,q} = \Delta i_{d,q}^* - \Delta i_{d,q} \tag{11}$$

where Δu_dc^* is the reference signal of the dc-bus voltage of the PVC, $\Delta i_{d,q}$ is the grid-connected current in the d-axis and q-axis, $\Delta i_{d,q}^*$ is the reference of the inner loop.

Each intermediate variable of the controller can be calculated as

$$\begin{cases} \Delta i_d^* = K_\mathrm{pv}(\Delta u_\mathrm{dc} - \Delta u_\mathrm{dc}^*) + K_{iv}X_v, \Delta i_q^* = 0 \\ \Delta m_{d,q} = K_{pi}(\Delta i_{d,q}^* - \Delta i_{d,q}) + K_{ii}X_{id,q} + u_{d,q} \\ \qquad \mp\omega(L_1 + L_2)\Delta i_{q,d} \end{cases} \tag{12}$$

where K_pv and K_{pi} are the proportionality coefficients in voltage and current loop, K_{iv} and K_{ii} are the integral coefficients and $\Delta u_{d,q}$ is the grid-connected voltage in the d-axis and q-axis, and $\Delta m_{d,q}$ is the modulating voltage signal in d-axis and q-axis.

On this basis, the controller can be modeled in (13) with a small-signal HTM

$$\begin{cases} sX_C = A_C X_C + B_C U_C \\ Y_C = C_C X_C + D_C U_C = [\Delta \mathrm{sw}_a, \Delta \mathrm{sw}_b, \Delta \mathrm{sw}_c]^T \\ X_C = [\Delta X_\mathrm{v}, \Delta X_{id}, \Delta X_{iq}]^T \\ U_C = [\Delta i_{ga}, \Delta i_{gb}, \Delta i_{gc}, \Delta u_\mathrm{dc}, \Delta u_{ga}, \Delta u_{gb}, \Delta u_{gc}]^T \end{cases} \tag{13}$$

where A_C and B_C are the state and input matrix of the controller state space model.

Similar to the topology model, sX_C can also be considered zero in the linearization period. The HTM between the switching function and grid-connected voltage or current can be rewritten

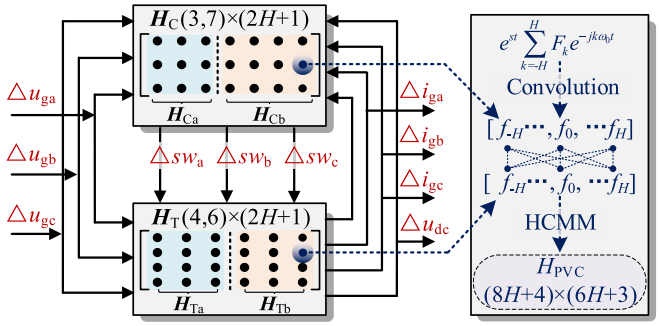

Fig. 3. Modeling process of HCMM.

as (15)

$$H_C = (-(A_C - N)^{-1}B_C + D_C)U_C = H_{Ca} + H_{Cb} \quad (14)$$

where H_{Ca} and H_{Cb} are the separate transfer matrices of voltage and current.

Therefore, the HSS controller model of PVC in (16) can be obtained following (15) to represent the relationship between the switching function and grid-connected voltage or current

$$\begin{pmatrix} \Delta \mathrm{sw}_a \\ \Delta \mathrm{sw}_b \\ \Delta \mathrm{sw}_c \end{pmatrix} = H_{Ca} \begin{pmatrix} \Delta u_{ga} \\ \Delta u_{gb} \\ \Delta u_{gc} \end{pmatrix} + H_{Cb} \begin{pmatrix} \Delta i_{ga} \\ \Delta i_{gb} \\ \Delta i_{gc} \\ \Delta u_{\mathrm{dc}} \end{pmatrix}. \quad (15)$$

C. HCMM Modeling

To establish the harmonic coupling relationship between the grid-connected voltages and currents of PVC based on Sections II-A and Section II-B, Fig. 3 shows the connection between H_C and H_T to obtain the HCMM.

The switching function $\Delta \mathrm{sw}_x$ is regarded as constant in two continuous control cycles. Therefore, the PVC can be expressed in (17) by associating (10) and (16). Obviously, the outer characteristic of PVC is a multiple-input multiple-output system. Every value in the $(8H+4)\times(6H+3)$ matrix H_{PVC} characterizes the relationship between voltage and current at the chosen frequency

$$\begin{pmatrix} \Delta i_{ga} \\ \Delta i_{gb} \\ \Delta i_{gc} \\ \Delta u_{dc} \end{pmatrix} = \underbrace{(I - H_{Tb}H_{Ca})^{-1}(H_{Ta} + H_{Tb}H_{Cb})}_{H_{\mathrm{PVC}}} \begin{pmatrix} \Delta u_{ga} \\ \Delta u_{gb} \\ \Delta u_{gc} \end{pmatrix}. \quad (16)$$

To analyze the harmonic coupling characteristic in a selective phase, the HCMM of any phase in (16) can be rewritten as (17). The transfer relationship between voltage and current at the same frequency is described by the diagonal harmonic admittance $Y_{x,x}$. Distinguishing from traditional models, the matrix operation between H_C and H_T involving interactions between different frequencies expresses the fact that the non-diagonal admittance $Y_{x,y}$ of HCMM is not zero anymore. In addition, the harmonic coupling characteristics described by the HCMM can be used to analyze any other control and topology structures

TABLE I
TOPOLOGY AND CONTROLLER PARAMETERS

Parameter/Unit	Value	Parameter	Value
L_1/mH	2.0	K_{pv}	2
L_2/mH	0.5	K_{iv}	50
C/uF	20.0	K_{pi}	10
C_{dc}/uF	2×10^3	K_{ii}	200

$$\begin{bmatrix} \Delta i_{g,1} \\ \vdots \\ \Delta i_{g,x} \\ \vdots \\ \Delta i_{g,H} \end{bmatrix} = \begin{bmatrix} Y_{1,1} & \cdots & Y_{x,1} & \cdots & Y_{H,1} \\ \vdots & \ddots & \vdots & \ddots & \vdots \\ Y_{1,x} & \cdots & Y_{x,x} & \vdots & Y_{H,x} \\ \vdots & \ddots & \vdots & \ddots & \vdots \\ Y_{1,H} & \cdots & Y_{x,H} & \cdots & Y_{H,H} \end{bmatrix} \begin{bmatrix} \Delta u_{g,1} \\ \vdots \\ \Delta u_{g,x} \\ \vdots \\ \Delta u_{g,H} \end{bmatrix}. \quad (17)$$

III. Harmonic Coupling Analysis of the PI Parameters in PVC Control

Multiple groups of experiments on a PVC are designed in this section to obtain accurate admittance and verify the control influence on the harmonic coupling characteristics. The admittance amplitude is obtained by frequency scanning experiments. Then, the effect of control parameters on the admittance is analyzed, and the key parameter with a high degree of influence is selected. The final step is to express the law of selected parameter changes on different frequency bands, which provides a reference for parameter tuning. Table I gives the topology and initial controller parameters.

First, frequency scanning experiments are used to obtain the admittance amplitude of the HCMM. The experimental procedures are as follows. The first step is to record the harmonic current at each frequency for the ideal grid condition. In the second step, the $(6k \pm 1)$th background harmonic voltage of a single frequency is added to the sinusoidal supply voltage one by one, and the measured harmonic current at each frequency is also recorded in six groups. According to the IEEE standard for harmonic ranges in 380 V distribution systems [23], the percentage of fifth and seventh background harmonics is configured as 5%, and the percentage of remaining frequencies is 2%. The experimental results in the two steps are subtracted to express the harmonic current due to additional background harmonic voltage, and the assumption in this section is that the two harmonic components are linearly calculated. The third step makes admittance calculations of a column in HCMM by dividing the harmonic current after subtraction with the corresponding harmonic voltage. Since the harmonic currents of the PVC in ideal operation are considered, the admittance results obtained in this way are more accurate compared with the direct calculations with the grid-connected voltage and current. Fig. 4 shows the harmonic admittance results within 20th harmonics.

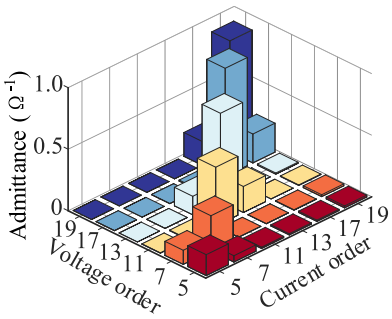

Fig. 4. Experimental results of harmonic admittance.

TABLE II
CONDITIONS WITH DIFFERENT CONTROLLER PARAMETERS

Case	Parameter	Case	Parameter
I	$0.5K_{pv}$	V	$0.5K_{pi}$
II	$1.5K_{pv}$	VI	$1.5K_{pi}$
III	$0.5K_{iv}$	VII	$0.5K_{ii}$
IV	$1.5K_{iv}$	VIII	$1.5K_{ii}$

Generally, high-frequency harmonics are suppressed by the *LCL* filter located on the PVC terminal, stronger harmonic coupling characteristics exist in the low pass band of the PVC filter. The experimental results show that the coupling admittance between $(6k-1)$th and $(6k+1)$th harmonics are larger than other frequencies, whereas k should take the same value. Among them, the percentage of coupled harmonics is 31.7% ($k=1$), 25.2% ($k=2$) and 19.2% ($k=3$), respectively. Therefore, this article is more focused on the coupling and mitigation characterization within 20th harmonics. However, not strong coupling phenomena exist in all frequencies, especially the coupling degree between non-diagonal frequencies is relatively small and can almost be neglected.

Furthermore, harmonic coupling characteristics are influenced by control parameters. Therefore, this section sets several groups of comparative experiments with different control parameters to analyze their coupling harmonic contribution. Experimental conditions are given in Table II, whose variation is based on the basic cases in Table I.

The variation of the harmonic admittance with different control parameters is defined in (18). The superscripts "I" and "II" denote the results measured in Tables I and II conditions, respectively,

$$\mathrm{HCE}=\frac{\left(Y_{x,y}^{\mathrm{II}}-Y_{x,y}^{I}\right)}{Y_{x,y}^{I}}\times 100\% \tag{18}$$

The metric in (13) characterizes the proportion of harmonic admittance change due to control parameter variation. A larger HCE means the corresponding control parameter has a higher degree of influence on the harmonic admittance. Fig. 5 shows the detailed experimental results for harmonic admittance in different frequencies. The relatively large range of HCE fluctuations is gathered in the conditions where K_{pi} is changed. The other three parameters have almost no effect on the harmonic admittance,

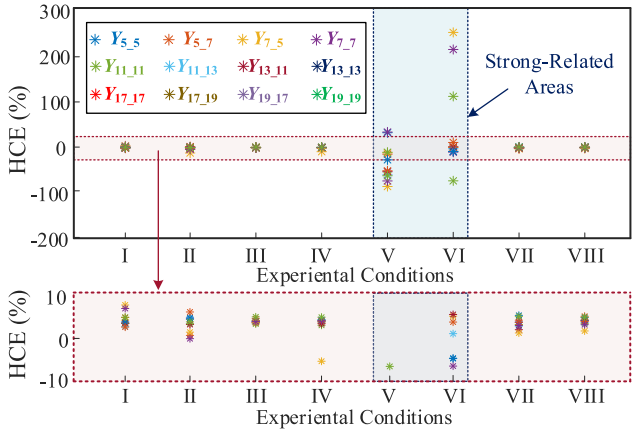

Fig. 5. Experimental results of different control parameters.

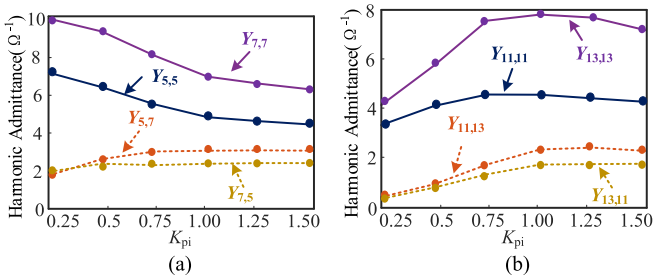

Fig. 6. Harmonic admittance under different values of K_{pi}. (a) 5th and 7th admittance (b) 11th and 13th admittance.

with HCE fluctuations less than 10%. Meanwhile, the neglected harmonics do not change significantly due to the variation of the control parameters.

Choosing the proper controller parameters is critical in distribution systems containing background harmonic voltages to reduce the harmonics during PVC operation. To analyze the more detailed relationship between the current-loop proportionality coefficient K_{pi} and the harmonic admittance, additional experiments have been done. With other parameters constant, K_{pi} in these experiments varies from 0.25 to 1.5 with a step of 0.25 under the basic parameters in Table I. Fig. 6 shows the $(6k\pm1)$th harmonic admittance under these cases.

Generally, the purpose of the current loop design is to provide sufficient *bandwidth* to ensure the current control response quickly and accurately. In addition, a more significant proportional gain means that the current loop has a higher *bandwidth* to track the reference signal faster. Therefore, under the premise of maintaining stable system operation, K_{pi} should be chosen as high as possible in the traditional perspective.

However, Fig. 6 shows that PVC presents different characteristics in diverse frequency bands. The remaining six admittance increase to various degrees with the increment of K_{pi} except for $\mathrm{Y}_{5,5}$ and $\mathrm{Y}_{7,7}$. Therefore, there are two entirely distinct choices for parameter tuning under the perspective of harmonic mitigation. A higher K_{pi} remains suitable for the conditions that the supply voltage contains low-frequency harmonic components. However, since the high-frequency admittance of PVC is

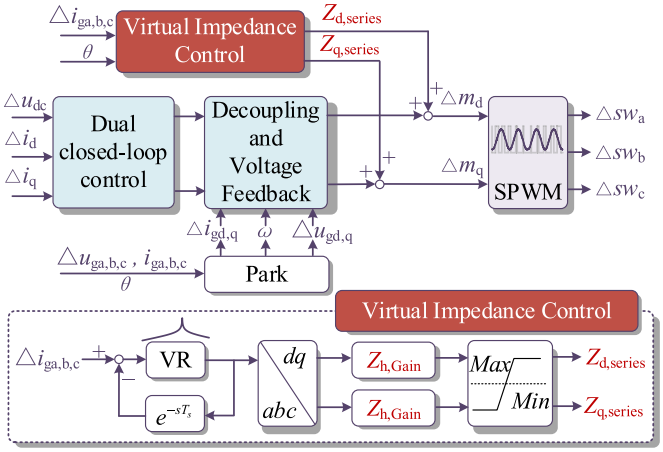

Fig. 7. Control diagram of virtual impedance.

high enough to create a significant harmonic current even under 1% corresponding harmonic voltage. Therefore, decreasing the *bandwidth* is a more reasonable choice when the grid voltage contains a certain percentage of high-frequency harmonics. The different harmonic characteristics increase the difficulty of parameter tuning.

IV. Harmonic Coupling Analysis for Virtual Impedance Control of PVC

Virtual impedance control is an effective method to suppress the low-frequency harmonic currents of the PVC. In this section, the influence of the $(6k \pm 1)$th virtual impedance on the harmonic admittance in the coupled frequency band is analyzed through multiple experiments with background harmonic voltage. After adding virtual impedance at the selective frequency, the measurement steps of harmonic admittance are consistent with Section III.

In previous research, proportional resonance, quasi-proportional resonance, or vector resonance (VR) controllers are used to extract the expected harmonic components [15]. The VR controller with better selectivity and harmonic tracking performance is used in this article. After adding the current feedback signal of the selected frequency to the modulating voltage reference signal, an equivalent selective series virtual impedance is constructed to the external characteristic of the PVC. Fig. 7 shows the control diagram of virtual impedance.

Generally, the influence of virtual impedance control on the PVC is to establish an approximate ideal equivalent series harmonic impedance. However, it must be emphasized that the constructed virtual impedance not only changes the harmonic characteristic at the selected frequency but also affects the coupling frequency, which has been neglected in previous studies. As illustrated in Section III, the percentage of harmonic coupling reaches 20%–30%, which should be emphasized in the mitigation work. Comparative experiments are designed to analyze the synchronous change of coupling harmonic admittance due to virtual impedance control. The amplitude of the selective virtual

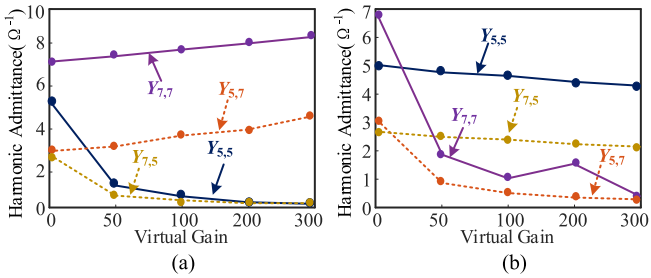

Fig. 8. Harmonic admittance between 5th and 7th harmonics.

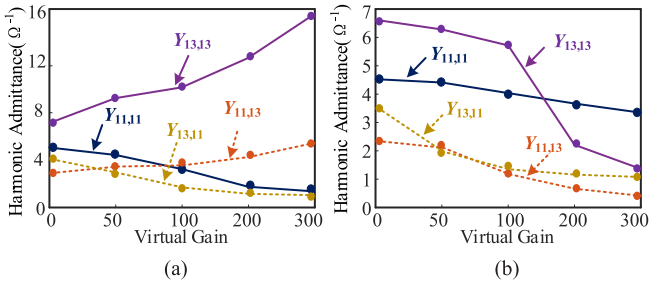

Fig. 9. Harmonic admittance between 11th and 13th harmonics.

impedance is determined by setting the virtual gain $Z_{h,\mathrm{Gain}}$ of feedback current.

Fig. 8(a) and (b) shows the measured harmonic admittance with fifth or seventh virtual impedance, respectively. The virtual gain of this section is set from 0 to 300 to ensure the stability of the PVC. The experimental results show that the fifth virtual impedance decreases $Y_{5,5}$ and $Y_{7,5}$ but increases $Y_{7,7}$ and $Y_{5,7}$. In contrast, the seventh virtual impedance suppresses $Y_{m,n}$ ($m, n = 57$) without generating extra fifth and seventh harmonic currents. Due to the harmonic admittance increasing with frequency, the 11th and 13th harmonic impedances are verified with 2% harmonic voltage. Fig. 9(a) and (b) are the harmonic admittance results with the 11th or 13th virtual impedance, respectively. A similar phenomenon can be obtained that $Y_{11,13}$ and $Y_{13,13}$ are increased due to the 11th virtual impedance. However, the harmonic admittance amplitude of other coupling frequencies decreases to different degrees.

In conclusion, the virtual impedance control does not simply change the self-harmonic admittance (SHA) of the PVC but has different contributions to the negative sequence coupled harmonic admittance (NSCHA), positive sequence coupled harmonic admittance (PSCHA), and coupled self-harmonic admittance (CSHA) simultaneously. Among them, the negative or positive sequence coupled harmonic admittance is separated by the frequency of the affected harmonic current. For example, $Y_{7,5}$ belongs to the negative sequence, and $Y_{5,7}$ belongs to the positive sequence. When $Y_{5,5}$ or $Y_{7,7}$ is defined as SHA, the other is the corresponding CSHA.

Fig. 10 shows the equivalent harmonic model considering the influence of virtual impedance on harmonic coupling. In this figure, "**Z**" donates the coupling characteristic due to a virtual impedance at the same frequency as the background

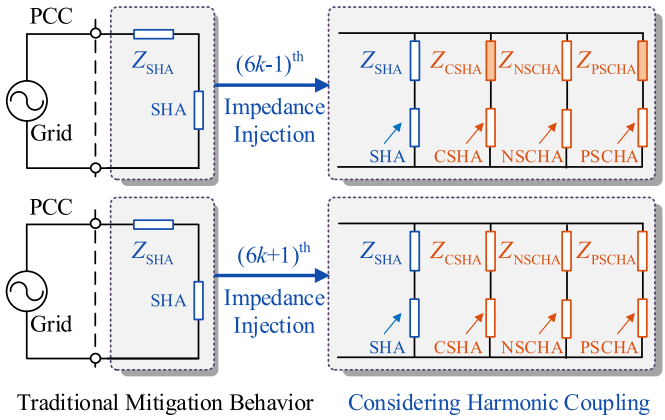

Fig. 10. Virtual impedance model considering coupling.

harmonic voltage, and the subscript means the affected admittance order. Furthermore, the impedance magnitude of the solid part is negative, which increases the corresponding harmonic admittance, resulting in more harmonic current in this supply condition. On the contrary, the hollow harmonic impedance magnitude is positive, which decreases the harmonic current. It can be seen from Fig. 10 that the amplitude of SHA is reduced by virtual impedance for the corresponding frequency, and the difference is reflected in the performance between the other three admittances. The $(6k-1)$th virtual impedance improves the PSCHA and CSHA, while the NSCHA is significantly decreased. However, the $(6k+1)$th virtual impedance suppresses all three harmonic admittance to different degrees.

In summary, constructing a virtual impedance at any selected frequency has an effect on four harmonic admittance in the coupling range. Therefore, the HCMM of PVC with virtual impedance control can be expressed in (19) with the premise that other frequencies are ignored, "**Y**" donates the coupled admittance submatrix when k takes a fixed value. Meanwhile, $\mathbf{Y}_{n,m}$ can be expressed in (20), and the subscript "m" or "n" means the affected harmonic admittance order, the superscript "m" or "n" is used to separate the contributions caused by virtual impedance at different frequencies

$$\begin{bmatrix} i_{g,5} \\ i_{g,7} \\ i_{g,11} \\ \vdots \\ i_{g,19} \end{bmatrix} = \begin{bmatrix} \mathbf{Y}_{5,7} & 0 & 0 \\ 0 & \mathbf{Y}_{11,13} & 0 \\ 0 & 0 & \mathbf{Y}_{17,19} \end{bmatrix} \begin{bmatrix} u_{g,5} \\ u_{g,7} \\ u_{g,11} \\ \vdots \\ u_{g,19} \end{bmatrix} \tag{19}$$

$$\begin{bmatrix} \frac{Y_{n,n}}{1+Y_{n,n}\left(Z^n_{SHA}+Z^m_{CSHA}\right)} & \frac{Y_{n,m}}{1+Y_{n,m}\left(-Z^n_{PSCHA}+Z^m_{PSCHA}\right)} \\ \frac{Y_{m,n}}{1+Y_{m,n}\left(Z^n_{NSCHA}+Z^m_{NSCHA}\right)} & \frac{Y_{m,m}}{1+Y_{m,m}\left(-Z^n_{CSHA}+Z^m_{SHA}\right)} \end{bmatrix}. \tag{20}$$

$$N=\{x=6k-1|k\in Z\},\quad n\in N, m=n+2$$

V. Coordinated Control of Adaptive Parameter Tuning and Virtual Impedance Injection

In the previous sections, the effect of control parameters and virtual impedance control on the coupled harmonic admittance are analyzed. To suppress harmonic currents in a nonideal power supply environment with random background harmonic voltages, a coordinated control method of adaptive parameter tuning and virtual impedance injection is proposed in this section. The proposed method requires fast and accurate separation of the harmonic voltage and current components. Therefore, the discrete Fourier transform (DFT) algorithm is used to obtain harmonic amplitudes with a sliding window whose length is 0.02 s. Furthermore, the adaptive control is divided into two steps as follows.

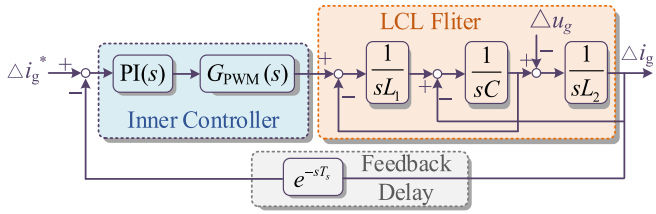

Fig. 11. Simplified inner loop controller model of the PVC.

1) *Current-Loop Proportionality Coefficient Tuning.* Compared with the coefficient K_{pi}, the effect of the remaining parameters on the harmonic admittance can be almost neglected. Therefore, a parameter optimization method is applied to decrease the total harmonic distortion (THD) rate of the PVC in Section V-A. The coefficient K_{pi} is iteratively calibrated based on the DFT result with the closed-loop system stable.
2) *Virtual Gain Tuning and Antisaturation Control*: Section V-B determines the virtual gain $Z_{h,\mathrm{Gain}}$ corresponding to the virtual impedance at each frequency. The delayed injection method of multiple frequency virtual impedance signals is used to avoid the instability of the system.

A. Step I: Current-Loop Proportionality Coefficient Tuning

Compared with the outer voltage loop, the inner current loop controller plays a more significant role in stability [24]. It is simplified as the model shown in Fig. 11 under the stable tracking of the dc voltage.

This section considers the current feedback and PWM calculation delays to make the final adjustment domain more accurate. The open-loop transfer function $G_{io}(s)$ and closed-loop transfer function $G_{ic}(s)$ in the S-domain are shown in (21) and (22), separately. In order to maintain the characterization accuracy while reducing the difficulty in modeling computational delays of digital controllers, an inertial segment is used to express the equivalent characteristics of delay. In this section, $T_s = 1e^{-4}$ s is the control cycle, and the inertia factor can be approximated as T_s

$$\begin{cases} G_{io}(s) = \frac{(K_{pi}+K_{ii}/s)G_{PWM}(s)}{s(s^2L_1L_2C+L_1+L_2)} \\ G_{PWM}(s) = e^{-sT_s} = \frac{1}{T_s s+1} \end{cases} \tag{21}$$

$$\begin{aligned} G_{ic}(s) &= \frac{G_{io}(s)}{1+G_{io}(s)e^{-sT_s}} = \frac{G_{io}(s)(T_s s+1)}{T_s s+1+G_{io}(s)} \\ &= \frac{(K_{pi}s+K_{ii})(T_s s+1)}{s^2(T_s s+1)^2(s^2L_1L_2C+L_1+L_2)+(K_{pi}s+K_{ii})}. \end{aligned} \tag{22}$$

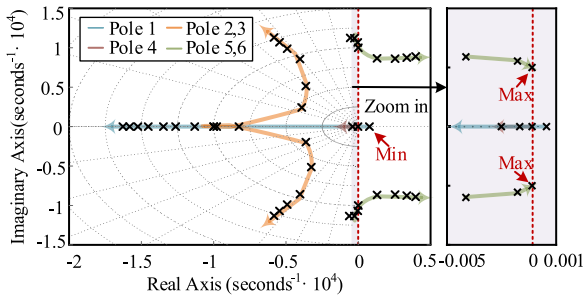

Fig. 12. Closed-loop dominate pole diagram of the G_{ic} (s).

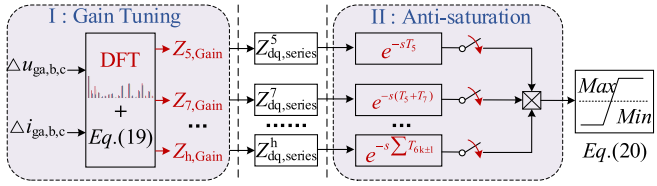

Fig. 13. Schematic diagram of the proposed method.

To quantify the adjustment domain of controller parameters, this section uses the root trajectory curve to determine the stabilization parameter boundaries. The closed-loop dominate pole diagram of the $G_{ic}(s)$ is shown in Fig. 12.

Six poles are classified into three categories based on their trajectories change with parameters. The first category contains a pair of conjugate poles indicated by the green line. They move to the right half plane as K_{pi} increases, and the critical value of its intersection with the imaginary axis determines the upper limit of the adjustment domain. The second category includes a pole of the blue line close to the real axis, it determines the lower limit of the adjustment domain because its real part will be larger than zero when K_{pi} is sufficiently small. The third category shows a pair of poles represented by the orange curve and a single pole shown by the red curve, which does not affect stability because they are both in the left half-plane. Therefore, the entire adjustment domain of the current loop proportionality coefficient in this section ranges from 0.024 to 15.838 after substituting the other parameters in Table I into consideration.

To reduce the harmonic content of PVC before adding a harmonic suppression strategy, the optimal current loop proportionality coefficient should be selected from the adjustment domain. The DFT results are used as a criterion for parameter adjustment and iterated every ten complete cycles until the constraints shown in (23) were satisfied

$$\begin{aligned} &K_{pi}^{k+1} = K_{pi}^{k} + \Delta K_{pi}, \mathrm{THD}_i = \sqrt[h]{\textstyle\sum_{m=2}^{h} i_m^2}/i_1. \\ &\text{s.t.} \quad \mathrm{THD}_i = \min \end{aligned} \tag{23}$$

It is appropriate to choose $K_{pi} = 10$ as the initial value in the stabilization range. Superscript "k" or "$k + 1$" means the number of iterations, and the iteration step size $\Delta K_{pi}$is set to 0.1 in this section. The controller parameter designed in this procedure results in the lowest output harmonics of PVC for the current power supply scenario, which somewhat reduces the proportion of subsequent virtual impedance injection.

B. Step II: Virtual Gain Tuning and Anti-Saturation Control

Obviously, the goal of virtual impedance injection is to achieve effective mitigation of harmonics at all frequencies. It is clear that the $(6k-1)$th virtual impedance causes the coupled harmonic increase instead of the $(6k+1)$th signals. Therefore, the sequences from $(6k-1)$th to $(6k+1)$th virtual impedance injection should be obeyed in the coupled harmonic mitigation process. It is divided into the following two steps.

1) $(6k-1)$th *Virtual Impedance Design*: To improve the efficiency of virtual impedance design, a suitable initial value is necessary in the optimization process. The results of Figs. 8 and 9 show that the harmonic suppression efficiency is higher when the virtual gain takes the value from zero to fifty, so fifty is the initial value set in this section. Then, the virtual gain grows flowing (24) until the percentage of the negative sequence harmonic current is less than 0.5%. Every time the gain increases, it should ensure the relative error in the harmonic amplitude of the corresponding frequency is less than 5% for at least three continuous waves. Where $\Delta Z_{\mathrm{Gain}} = 10$ is the step size for virtual gain iteration, and the superscript "n" or "0" is used to characterize the number of iterations

$$\begin{cases} Z_{h,\mathrm{Gain}}^{n} = Z_{h,\mathrm{Gain}}^{n-1} \pm \Delta Z_{\mathrm{Gain}} \\ Z_{h,\mathrm{Gain}}^{0} = 50 \end{cases}. \tag{24}$$

2) $(6k+1)$th *Virtual Impedance Design*. Similar to the $(6k-1)$th virtual impedance design, the $(6k+1)$th virtual gain also grows with the same span in (19) until the percentage of target positive sequence harmonic current is less than 0.5% equally.

Unlike closed-loop control methods, such as PI controllers, the series virtual impedance algorithm used in this article is open-loop control, which means the constructed signals directly change the final modulating voltage. A current fluctuation within a specific range will occur at the beginning of the open-loop control signal action, the relevant waveforms will be shown in Section VI. However, if the summation of the harmonic and fundamental modulation voltages reaches the limit of the modulation ratio of PVC, the grid-connected currents will enter an unstable state or may even destabilize the system due to receiving an erroneous modulation signal. Therefore, a multiple-frequency signals delayed injection method is adopted in this section to avoid the instability problem caused by the entrance of signals simultaneously. Fig. 13 shows the schematic diagram of the proposed method.

The multiple impedance signals are injected flowing (25) after the virtual gain tuning. Where T_μ is the delay for μth virtual impedance injection after the previous signal. It should be longer than the time to reach a new steady state after the action of the previous loop signals, which is recognized by a relative error of 5% for five continuous cycles in this section. The superscript "$\sim$"

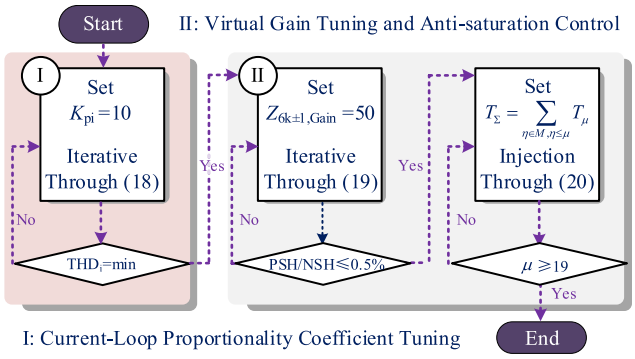

Fig. 14. Flow chart of the proposed method.

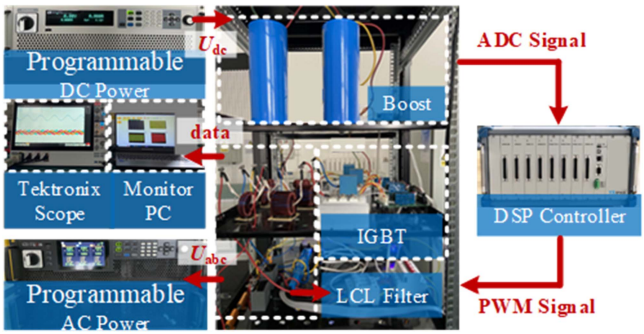

Fig. 15. Experimental platform.

means a previous state before multiple virtual impedance signals injection, and the superscript "μ" represents the harmonic order to be injected. Since the probability of the PVC overmodulation state is greatly reduced, the virtual impedance delay injection method can effectively improve the mitigation performance with minimal fluctuations. The flowchart of the proposed adaptive parameter tuning and virtual impedance injection method is shown in Fig. 14

$$\begin{cases} Z_{dq,\text{series}} = \sum\limits_{\mu\in M} Z^{\mu}_{dq,\text{series}} e^{-sT_\Sigma}, \quad T_\Sigma = \sum\limits_{\eta\in M,\eta\le\mu} T_\eta \\ M = \{x = 6k \pm 1 | k \in Z\} \\ \Delta m_{d,q} = Z_{dq,\text{series}} + \Delta\tilde{m}_{d,q} \subseteq \left(-\frac{u_{dc}}{2}, \frac{u_{dc}}{2}\right) \end{cases} . \tag{25}$$

VI. Experimental Conditions

Fig. 15 shows the PVC experimental platform and hardware in this paper with productized drivers carrying single-core digital signal processing (DSP) (TMS320F28335), its control and sampling frequency are both 10 kHz. PV is simulated by a programmable dc power, and the programmable ac power is used to provide the grid voltage and background harmonic conditions. The monitor PC reflects the variable status in real time, and data storage is accomplished by an oscilloscope whose bandwidth is 1 GHz. The RMS value of the grid-connected voltage in the following experiments is 110 V, and the PV power is 2 kW.

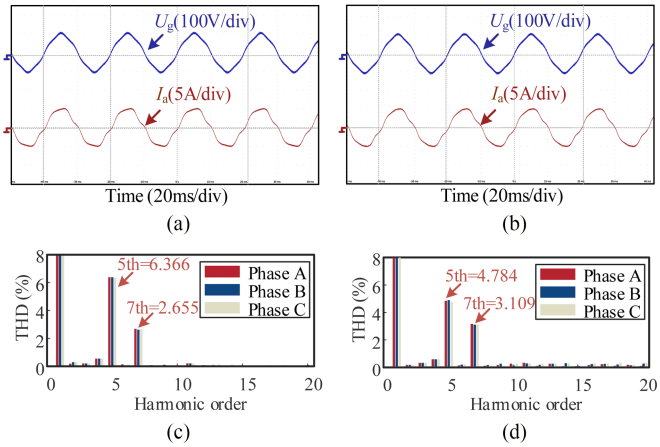

Fig. 16. Comparative results with 5% fifth harmonic voltage. (a) $K_{pi} = 5.0$. (b) $K_{pi} = 14.2$. (c) $K_{pi} = 5.0$. (d) $K_{pi} = 14.2$.

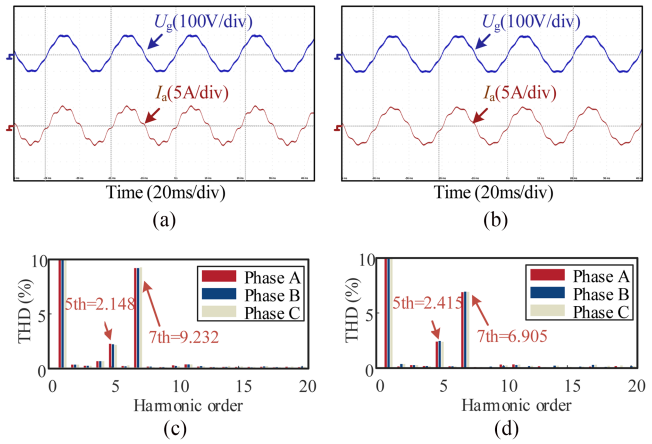

Fig. 17. Comparative results with 5% seventh harmonic voltage. (a) $K_{pi} = 5.0$. (b) $K_{pi} = 14.6$. (c) $K_{pi} = 5.0$. (d) $K_{pi} = 14.6$.

A. Current-Loop Parameter Optimization Experiments

Section VI-A compares the harmonic performance of the PVC after parameter tuning and the original data in different conditions. Fig. 16 shows the comparative results with 5% fifth background harmonic voltage, and Fig. 17 shows the case with the same percentage of seventh background harmonic. The experiments certify that it is reasonable to ignore the interaction between the weaker coupled frequencies in Fig. 4.

From Fig. 16, the fifth harmonic current decreases from 6.366% to 4.784%, while the seventh harmonic rises from 2.655% to 3.109%. The little amplitude error in fundamental frequency is ignored, and the THD rate after parameter tuning is reduced by 13% under the same cases. For the seventh harmonic, its rate decreases from 9.232% to 6.905% after parameter optimization, while the fifth harmonic rises from 2.148% to 2.415%. The THD rate is reduced by 19% after adopting the parameter iterative method proposed in this article. Therefore, parameter tuning can reduce harmonics to some extent, but it is difficult to achieve the desired harmonic mitigation. Under the supply conditions with 2% or 5% background harmonic voltage, the

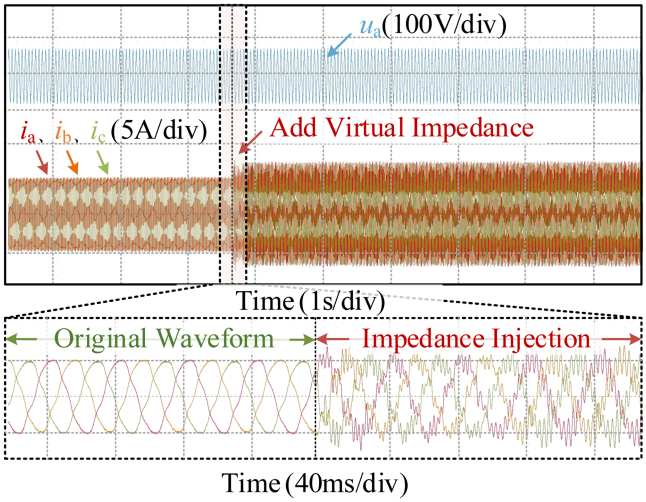

Fig. 18. Simultaneous signals injection experiment.

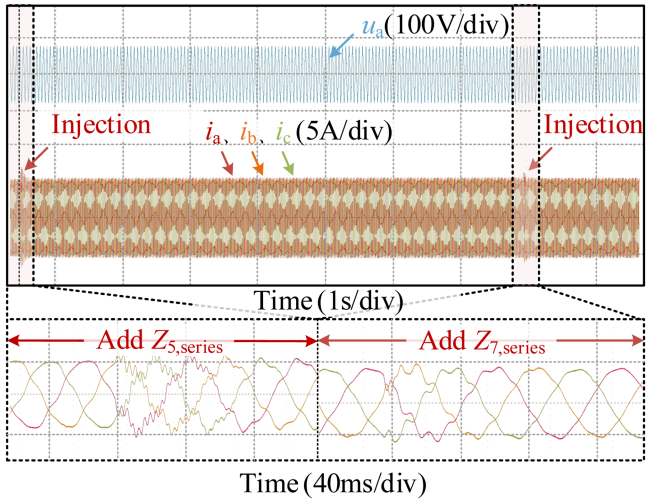

Fig. 19. Delayed signals injection experiment.

harmonic component in the grid-connected current of the PVC still exceeds the specified range. Additional virtual impedance is required for such nonideal conditions, and these experiments are shown in Section VI-B.

B. Antisaturation Experiments

In Section VI-B, the virtual impedance signals adjusted according to Section V will be injected into the controller at the same time or in segments to demonstrate the superiority of the delayed injection method proposed before. The same virtual gains are used to control the variables, and the supply voltage contains 5% fifth background harmonics.

The bandpass property of the VR controller determines that the small virtual gain works invalid. So when the open-loop control signals representing multiple virtual impedances are injected and overlayed with the modulating voltage reference signal simultaneously, the limit $\pm u_{dc}/2$ of the PWM may be reached. The following result is that the initially stable fundamental frequency control is broken. The grid-connected current of the PVC generates severe distortion in this undesirable state. This kind of signal injection mode makes harmonic suppression fail or even causes equipment to be removed in some grids with poor supply conditions.

As shown in Fig. 18, the amplitude of the grid-connected current increases significantly and oscillates due to multiple virtual harmonic impedance signals injection together. It should be emphasized that the PVC will not reach a new steady-state independently if the supply conditions and the control method are unchanged. In addition, impedance injection does not cause the current to go out of control. Instead, it puts the PVC in a state of distorted modulation where the fundamental and impedance frequency signals are constrained by each other. The stable state will eventually be broken due to the continuous increment of virtual impedance amplitude.

However, this problem of modulation voltage saturation can be significantly solved by adopting multiple virtual impedance signals delayed injection method proposed in Section V. Fig. 19 shows the antisaturation comparison experiment.

Although the disturbance over several control cycles due to open-loop signal injection remains unavoidable, the system quickly reaches a new steady state due to the existence of closed-loop control. The delayed injection method proposed in this article reduces the current fluctuation due to virtual impedance and avoids the risk of the system being over-modulated. Therefore, the advantage of the proposed method is avoiding multiple signals changing the modulation voltage resources segment, which in turn ensures the robustness of the fundamental frequency control. It should be mentioned that Section VI-B only verifies the transient stability characteristics of the control method. The influence on THD will be shown in Section VI-C.

C. Harmonic Mitigation Experiments

Section VI-C shows the coupled harmonic mitigation performances of the virtual impedance injection method proposed in Section V. Another purpose of these experiments is to verify the analysis of the virtual impedance algorithm on the coupled harmonic admittance in Section IV.

Figs. 20 and 21 show the waveforms of grid voltage and PVC current, fast Fourier transform results after the fifth and seventh virtual impedance signals injection. Compared with the parameter tuning results in Fig. 16, the fifth impedance injection increases the seventh harmonic current, and the percentage of coupled harmonics are both below 0.5% after injection of the seventh impedance continually.

The same conclusion can be obtained by comparing Figs. 22 with 17. The seventh harmonic in the grid-connected current of the PVC increases due to the fifth virtual impedance injection. This problem is effectively solved with the seventh virtual impedance injection. The mitigation rate of target harmonics is above 95%, and the proposed method has little influence on other components.

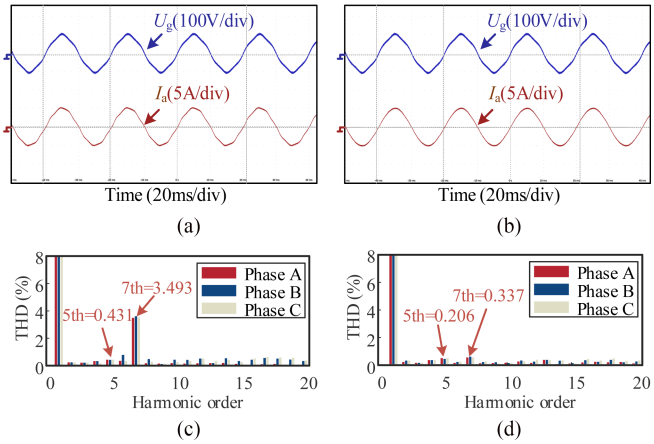

Fig. 20. Experiments with 5% fifth harmonic voltage. (a) 5th signal injection. (b) 7th signal injection. (c) 5th signal injection. (d) 7th signal injection.

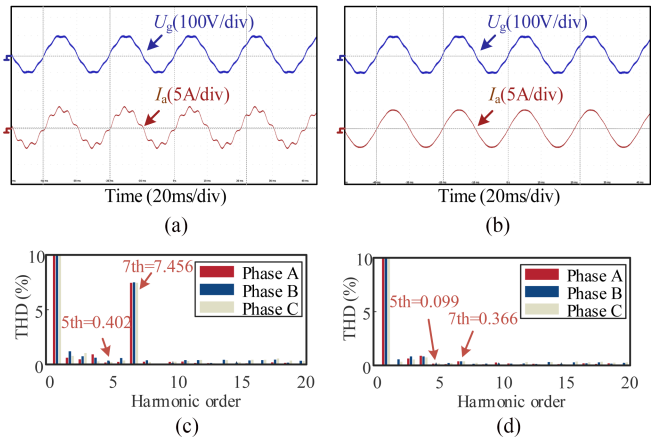

Fig. 21. Experiments with 5% seventh harmonic voltage. (a) 5th signal injection. (b) 7th signal injection. (c) 5th signal injection. (d) 7th signal injection.

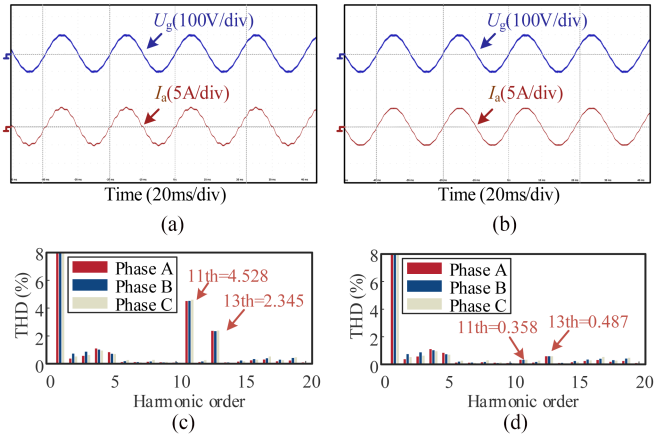

Fig. 22. Experiments with 2% 11th harmonic voltage. (a) Original waveform. (b) Proposed method. (c) Original data. (d) Proposed method.

The following experiments in Figs. 22 and 23 are shown to verify the harmonic suppression performance of the adaptive virtual impedance injection method at higher frequencies, which is higher than 500 Hz. From Fig. 4, the harmonic equivalent admittance increases with the frequency. In other words, PVC makes

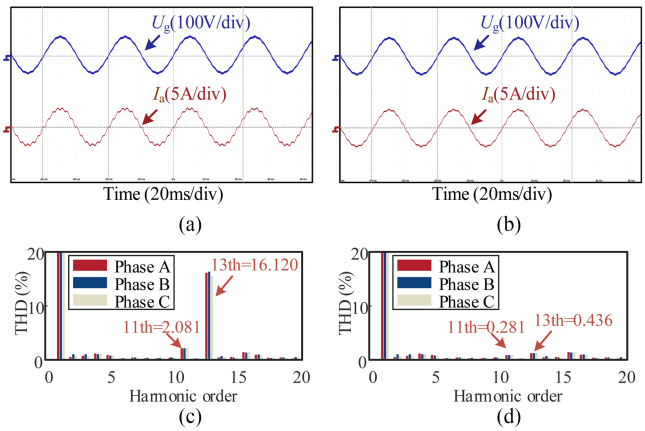

Fig. 23. Experiments with 2% 13th harmonic voltage. (a) Original waveform. (b) Proposed method. (c) Original data. (d) Proposed method.

more significant harmonic currents in cases with high-frequency background harmonic voltage, and the experimental results in this section also confirm this conclusion. In the supply condition shown in Fig. 22, the component of the 11th harmonic current grows to 4.58% due to only 2% voltage distortion. Even worse, the 13th harmonic rate reaches 16.12% in the next case with the same percentage of background harmonic voltage. Obviously, the excitation ratio is significantly larger than the low-frequency harmonics, which is lower than 500 Hz. The coupled harmonic contents can still be controlled within the desired range after the virtual impedance injection of the coupling frequency. Even the heavily distorted waveforms due to the existence of the 13th harmonic achieve a huge improvement in their sinusoidal degree.

From the comparative experiments in Section VI-C, the correctness of the coupled harmonic analysis is verified, and the conclusion can be drawn that the constructed virtual impedance can effectively suppress the coupled harmonics of PVC. The proposed injection method from $(6k-1)$th to $(6k+1)$th virtual impedance improves the efficiency of suppressing coupled harmonics without any negative impact on other frequencies. Meanwhile, it also avoids the problem of increasing nontarget frequency harmonics due to unreasonable virtual impedance injection. Therefore, the optimum harmonic mitigation performance can be obtained by injecting the smallest coupled virtual impedance signals, maximizing the ability of the system to operate stably.

D. Dynamic Harmonic Mitigation Experiments

Section VI-D shows the dynamic harmonic mitigation performance under different power conditions. Fig. 24 shows the comparative results with 5% fifth background harmonic voltage, and the experimental power conditions are 1.5, 2, and 2.5 kW separately.

The dynamic progress in Fig. 24 can be divided into five stages. The first one is the original grid-connected current waveform under supply condition with voltage distortion, the same experimental results have been shown in Fig. 16. The second and third stages separately represent step I and step II

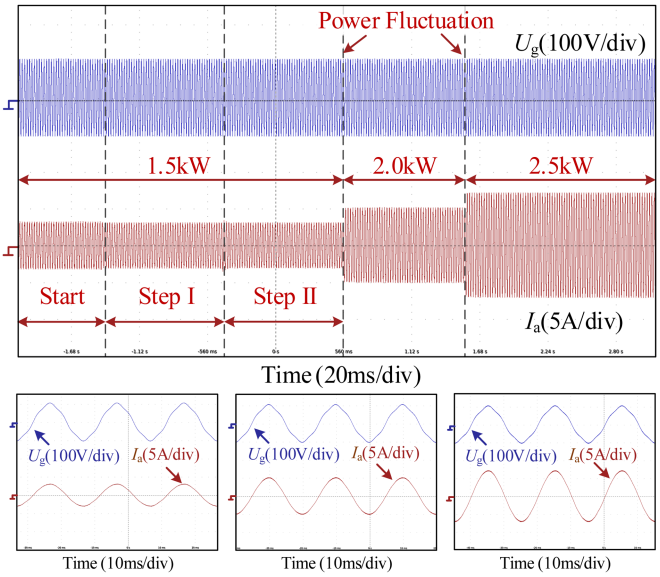

Fig. 24. Dynamic harmonic mitigation performance under different power conditions.

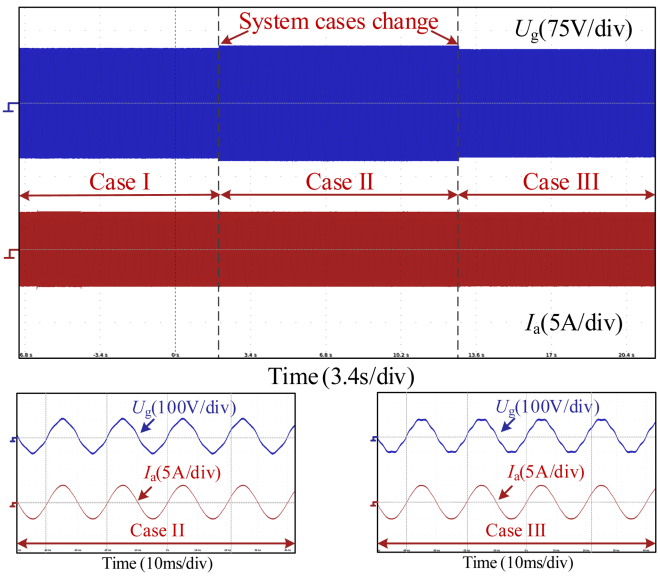

Fig. 25. Dynamic harmonic mitigation performance under different power conditions.

of the virtual impedance tunning and injection method which is shown in Fig. 13. The fourth and fifth stages represent the dynamic harmonic mitigation performance in power fluctuation conditions, respectively.

Since the grid supply condition is stable and the harmonic impedance of PVC does not change due to power fluctuations, the grid-connected current can maintain a sinusoidal waveform in a variable PV generation system due to the mitigation method proposed in this article. Furthermore, the experiments shown in Fig. 25 validate the dynamic mitigation performance under conditions of background harmonic changes. In case I, the RMS value of the grid-connected voltage is 110 V, and the PV power is

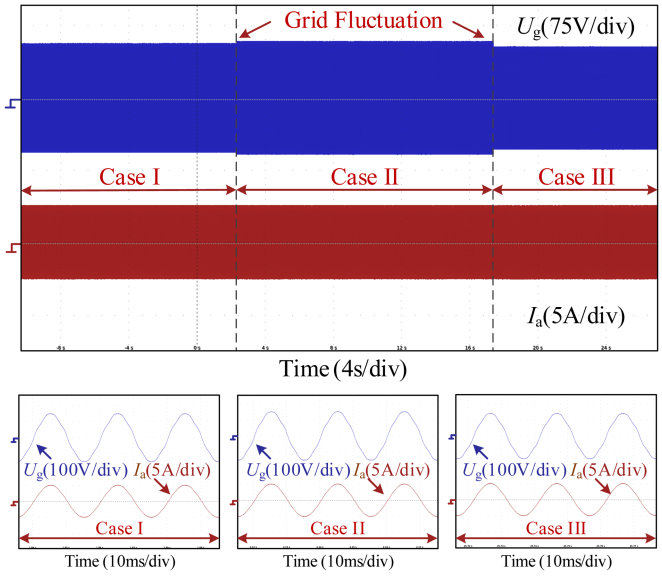

Fig. 26. Dynamic harmonic mitigation performance under grid fluctuation conditions.

2 kW. Case II and case III add 5% fifth harmonic or 5% seventh harmonic to the grid voltage separately.

The experimental results show that if the background harmonic condition changes, the PVC can still guarantee a low current THD by executing once again the virtual impedance tuning and adjustment process shown in Fig. 13. Furthermore, Fig. 26 shows the dynamic harmonic mitigation performance under conditions of grid fundamental voltage changes. The grid condition contains 2.5% fifth and seventh harmonic voltages, and the RMS values of fundamental voltage in case I, case II, and case III are separately 106, 110, and 100 V. These experimental results show that the method proposed in this article can guarantee a high-quality current of PVC, whether the grid fundamental or harmonic voltage dynamic changed.

Generally, the power system supply conditions fluctuate over long time scales, and the system state can be seen as stable in several minutes or even a few hours, so frequent PVC harmonic impedance reshaping is not required for practical scenario applications. Adjustment only needs to occur where the system background harmonic state changes significantly from the original condition, which also avoids frequent operation of the PVC.

VII. Conclusion

Based on the HCMM, the harmonic coupling phenomenon and the coupled mitigation behavior of virtual impedance are discussed. The discoveries and innovations are as follows.

1) There is a significant harmonic coupling between the $(6k \pm 1)$th voltages and currents of PVC. The harmonic admittance increases, but the coupling severity decreases significantly with increasing k. The percentage of coupling components is 31.7% ($k = 1$), 25.2% ($k = 2$), and 19.2% ($k = 3$), respectively.
2) The proportionality coefficient K_{pi} has the most significant effect on harmonic admittance. A higher bandwidth of the

inner loop is more suitable for the grid with low rather than high-frequency background harmonics.

3) Virtual impedance control does not exhibit a desirable SHA characteristic. The $(6k-1)$th virtual impedance signals decrease mitigation behavior in the $(6k+1)$th harmonic currents, but the $(6k+1)$th control will not aggravate the $(6k-1)$th harmonic currents.
4) The proposed method guarantees coupled harmonic currents less than 0.5% under nonideal conditions with complex background harmonic voltage. Moreover, the robustness of the control system can be ensured by multiple impedance signals delayed injection.

The adaptive parameter tuning and virtual impedance injection control for coupled harmonic mitigation proposed in this article helps improve the ability of PVC to consistently provide high-quality power under nonideal conditions. Furthermore, it can also be widely extended to the grid containing a high percentage of new energy to improve the power quality. Future research will focus on the influence analysis on the coupled harmonic interactions with multiple PVCs and harmonic suppression methods according to the harmonic coupling characteristic of the single PVC.

REFERENCES

[1] Y. Li, Y. Sun, Q. Wang, K. Sun, K. Li, and Y. Zhang, "Probabilistic harmonic forecasting of the distribution system considering time-varying uncertainties of the distributed energy resources and electrical loads," *Appl. Energy*, vol. 329, Jan. 2023, Art. no. 120298.

[2] B. Pang, X. Zhu, J. Yang, K. Liao, B. Chen, and Z. He, "Voltage harmonics optimization for weak grid-tied doubly-fed induction generator with the capability of suppressing current harmonics," *IEEE Trans. Energy Convers.*, vol. 38, no. 2, pp. 1452–1460, Jun. 2023.

[3] Q. Xu et al., "A generalized admittance criterion for dominant harmonic source determination without synchronous phasor measurements," *Int. J. Elect. Power Energy Syst.*, vol. 155, Jan. 2024, Art. no. 109481.

[4] Y. Wang, J. Tang, J. Si, X. Xiao, P. Zhou, and J. Zhao, "Power quality enhancement in islanded microgrids via closed-loop adaptive virtual impedance control," *Protection Control Modern Power Syst.*, vol. 8, no. 1, p. 10, 2023.

[5] Y. Liu et al., "Harmonic state space based impedance modeling and virtual impedance based stability enhancement control for LCC-HVDC systems," *J. Modern Power Syst. Clean Energy*, vol. 12, no. 1, pp. 287–298, Jan. 2024.

[6] W. U. K. Tareen and S. Mekhielf, "Three-phase transformerless shunt active power filter with reduced switch count for harmonic compensation in grid-connected applications," *IEEE Trans. Power Electron.*, vol. 33, no. 6, pp. 4868–4881, Jun. 2018.

[7] Z. Yang et al., "A system-level harmonic control method based on multi-bus voltage detected APF without exact phase synchronization," *IEEE J. Emerg. Sel. Top. Power Electron.*, vol. 11, no. 3, pp. 2618–2631, Jun. 2023.

[8] B. Gao, Y. Wang, and W. Xu, "An improved model of voltage source converters for power system harmonic studies," *IEEE Trans. Power Del.*, vol. 37, no. 4, pp. 3051–3061, Aug. 2022.

[9] D. Kumar and F. Zare, "Harmonic analysis of grid connected power electronic systems in low voltage distribution networks," *IEEE J. Emerg. Sel. Top. Power Electron.*, vol. 4, no. 1, pp. 70–79, Mar. 2016.

[10] C. Shang, M. Yang, J. Long, D. Xu, J. Zhang, and J. Zhang, "An accurate VSI nonlinearity modeling and compensation method accounting for DC-link voltage variation based on LUT," *IEEE Trans. Ind. Electron.*, vol. 69, no. 9, pp. 8645–8655, Sep. 2022.

[11] P. Shan, M. Yang, X. Li, C. Shang, J. Long, and D. Xu, "Online inverter nonlinearity compensation method based on current injection," in *Proc. 24th Int. Conf. Elect. Mach. Syst.*, 2021, pp. 1911–1916.

[12] Y. Qi, J. Fang, J. Liu, and Y. Tang, "Coordinated control for harmonic mitigation of parallel voltage-source inverters," *CES Trans. Elect. Mach. Syst.*, vol. 2, no. 3, pp. 276–283, Sep. 2018.

[13] Y. Liu. et al., "Coordinated mitigation control for wideband harmonic of the photovoltaic grid-connected inverter," *Appl. Sci.*, vol. 13, no. 13, Jun. 2023, Art. no. 7441.

[14] A. Terciyanli et al., "A current source converter-based active power filter for mitigation of harmonics at the interface of distribution and transmission systems," *IEEE Trans. Ind. Appl.*, vol. 48, no. 4, pp. 1374–1386, Jul./Aug. 2012.

[15] X. Wu, J. Lou, K. Sun, Y. Sun, P. Shan, and Q. Li, "Research on harmonic compensation control strategy considering capacity limitation of PV grid-connected inverter," in *Proc. 8th Asia Conf. Power Elect. Eng.*, 2023, pp. 1437–1442.

[16] Y. Li, J. He, Y. Liu, Y. Ren, and Y. W. Li, "Decoupled mitigation control of series resonance and harmonic load current for HAPFs with a modified two-step virtual impedance shaping," *IEEE Trans. Ind. Electron.*, vol. 70, no. 8, pp. 8064–8074, Aug. 2023.

[17] Y. Li, Y. Sun, K.-J. Li, K. Sun, Z. Liu, and Q. Xu, "Harmonic modeling of the series-connected multi-pulse rectifiers under unbalanced conditions," *IEEE Trans. Ind. Electron.*, vol. 70, no. 7, pp. 6494–6505, Jul. 2023.

[18] Y. Hu, Y. Shao, R. Yang, X. Long, and G. Chen, "A configurable virtual impedance method for grid-connected virtual synchronous generator to improve the quality of output current," *IEEE J. Emerg. Sel. Top. Power Electron.*, vol. 8, no. 3, pp. 2404–2419, Sep. 2020.

[19] M. A. Awal, H. Yu, I. Husain, W. Yu, and S. M. Lukic, "Selective harmonic current rejection for virtual oscillator controlled grid-forming voltage source converters," *IEEE Trans. Power Electron.*, vol. 35, no. 8, pp. 8805–8818, Aug. 2020.

[20] H. Zhou and L. He, "Impedance-edited multiple low-frequency harmonic current adaptive suppression," *IEEE Trans. Power Electron.*, vol. 38, no. 6, pp. 7022–7033, Jun. 2023.

[21] Y. Li, Y. Sun, K.-J. Li, J. Lou, K. Sun, and P. An, "Harmonic power flow calculation based on unified harmonic state-space model of converter," in *Proc. IEEE Ind. Appl. Soc. Annu. Meeting*, 2022, pp. 1–7.

[22] J. Kwon, X. Wang, F. Blaabjerg, C. L. Bak, V.-S. Sularea, and C. Busca, "Harmonic interaction analysis in a grid-connected converter using harmonic state-space (HSS) modeling," *IEEE Trans. Power Electron.*, vol. 32, no. 9, pp. 6823–6835, Sep. 2017.

[23] *IEEE Standard for Interconnection and Interoperability of Distributed Energy Resources With Associated Electric Power Systems Interfaces*, IEEE Std 1547-2018, 2018.

[24] C. Shang, M. Yang, and J. You, "High bandwidth current regulator design for PMSM based on frequency sweep correction," *IEEE Trans. Ind. Electron.*, vol. 71, no. 2, pp. 1768–1778, Feb. 2024.

Pengbo Shan (Student Member, IEEE) received the B.S. and M.S. degrees in electrical engineering from the Harbin Institute of Technology, Harbin, China, in 2019 and 2022, respectively. He is currently working toward the Ph.D. degree in electrical engineering with Shandong University, Jinan, China.

His research interests include control algorithms for harmonic mitigation.

Yuanyuan Sun (Senior Member, IEEE) received the B.S. and Ph.D. degrees in electrical engineering from the School of Electrical Engineering, Shandong University, Jinan, China, in 2003 and 2009, respectively.

She is currently a Professor with the School of Electrical Engineering, Shandong University. Her research interests include harmonic modeling and analysis and active distribution system.

Yuanzong Song received the B.S. degree in electrical engineering from the Changchun University of Science and Technology, Changchun, China, in 2022. He is currently working toward the M.S. degree in electrical engineering with Shandong University, Jinan, China.

His research interests include control strategies for converters.

Fan Zhang received the B.Sc. and Ph.D. degrees in electrical engineering from Shandong University, Jinan, China, in 2003 and 2008, respectively.

He was the Leader of R&D Department, China Electric Power Research Institute, the Head of Technical Department in Big Data Center of SGCC and the Global Energy Interconnection Research Institute, China. He is currently the Head of the Department of Science and Technology Innovation, China Electrical Equipment Group Co., Ltd., Nanjing, China. He mainly focused on the power system relay protection, power electronics, smart distribution network, big data analysis of electric power etc.

Yahui Li (Member, IEEE) received the B.S. and M.S. degrees from Northeast Electric Power University, Jilin, China, in 2015 and 2018, respectively, and the Ph.D. degree in electrical engineering from Shandong University, Jinan, China, in 2023.

He is currently a PostDoctor with Shandong University, Jinan, China. His research interests include power quality analysis and harmonic modeling.

Kaiqi Sun (Member, IEEE) received the B.S. and Ph.D. degree in electrical engineering from Shandong University, Jinan, China, in 2015 and 2020, respectively.

He is currently a Visiting Scholar with the University of Tennessee, Knoxville, TX, USA, from 2017 to 2020. From 2020 to 2021, he was a Research Associate with the Department of Electrical Engineering and Computer Science, University of Tennessee, Knoxville, TN, USA. He is currently an Associate Research Fellow with Shandong University. He has authored or coauthored more than 50 peer-reviewed technical articles or conference papers. His research interests include the HVDC and MVDC system operation, renewable energy integration and machine learning based power system application.

Dr. Sun is the recipient of the Best Paper Award from IEEE IAS Industrial and Commercial Power System Asia Asia, ECAI and the SCEMS 2020.